



# Reconstruction and quantitative characterization of the three dimensional microstructure model of TC6 titanium alloy based on dual-energy X-ray microtomography

Guoju Li<sup>a,b</sup>, Ran Shi<sup>a,b</sup>, Qunbo Fan<sup>a,b,\*</sup>, Yumeng Xia<sup>a,b</sup>, Hongmei Zhang<sup>a,b</sup>

<sup>a</sup> National Key Laboratory of Science and Technology on Materials Under Shock and Impact, Beijing 100081, China

<sup>b</sup> School of Materials Science and Engineering, Beijing Institute of Technology, Beijing 100081, China

## ARTICLE INFO

### Article history:

Received 28 July 2016

Received in revised form

14 August 2016

Accepted 18 August 2016

Available online 20 August 2016

### Keywords:

Electron microscopy

EBSD

Tomography

Microanalysis

Titanium alloys

## ABSTRACT

In the present study, dual-energy micro-computed tomography (Micro-CT) imaging was employed to overcome the difficulty of low absorption contrast due to the low difference in density among the primary  $\alpha$  phase, secondary  $\alpha$  phase, and  $\beta$  phase of the annealed microstructure (annealing at 800 °C for 2 h followed by air cooling) of TC6 titanium alloy. The three dimensional microstructure model of TC6 titanium alloy was first achieved by laboratory X-ray microtomography, and then analyzed quantitatively. It is found that the volume fractions of the primary  $\alpha$  phase, secondary  $\alpha$  phase and  $\beta$  phase are 28.32%, 47.78% and 23.90%, respectively. Some complex microstructural features of TC6 titanium alloy such as spatial distribution, shapes, and interconnectivities that can hardly be described by the conventional two dimensional microscopy technique were successfully captured. In three dimensional space, the primary  $\alpha$  phase is composed of discrete equiaxed grains and interconnected grains, and the fraction of the individual equiaxed grains is up to 50% and the average diameter is about 10  $\mu\text{m}$ ; the secondary  $\alpha$  phase interconnects with  $\beta$  phase forming a completely interconnected network.

© 2016 Elsevier B.V. All rights reserved.

## 1. Introduction

Owing to its attractive properties such as high specific stiffness and strength, excellent anti-fatigue performances, and resistance to crack propagation compared with other lightweight alloys and steel and nickel alloys; dual-phase ( $\alpha + \beta$ ) titanium alloys have found many key applications in aerospace and industry [1,2]. It is widely recognized that the properties of the alloys strongly depend on the microstructure features of each constituent phase, such as volume fraction, size, and morphology [3,4]. Hence, quantitative three-dimensional (3D) characterization of the microstructures is fundamental. However, using traditional metallographic techniques, the complex microstructural features including the spatial distribution, intrinsic shape, and interconnectivities of the existing phases can hardly be described by the observation of two-dimensional (2D) planar sections [5,6]. With the establishment of serial sectioning method [7,8], the 3D microstructure model in a wide variety of materials can be reconstructed via the controlled repetition of 2D sectioning techniques. However, the

widespread use of metals and alloys is limited, owing to the involvement of various surface finishing operations, such as grinding, polishing, corroding, and metallographic observation, which not only destroys the inherent microstructural morphology, but also makes the process tedious and time consuming [9,10]. With considerable improvements in the quality and performance of X-ray tubes, as well as high-resolution flat-panel matrix detectors, X-ray microtomography capable of high-resolution, non-destructive, and high-efficiency imaging techniques has become an accepted tool for the acquisition of 3D microstructure images of materials [11,12]. Based on the difference in X-ray source, X-ray microtomography can be divided into two categories: synchrotron and laboratory. Recently, synchrotron X-ray microtomography, which possesses the significant advantages of a monochromatic and parallel beam with high brilliance, has been applied for the acquisition of 3D microstructure images of metals and alloys. Maire [13], Vanderesse [9], and Singh [14] obtained the 3D microstructure images of the constituent phases of 5182 aluminum alloy, TA6V dual-phase titanium alloy, and 7075 aluminum alloy by synchrotron X-ray absorption tomography. Clearly, laboratory X-ray microtomography gives much wider availability and accessibility than synchrotron X-ray microtomography. It has been used in rocks and porous ceramics [15–19] as well as composites [20–

\* Corresponding author at: School of Materials Science and Engineering, Beijing Institute of Technology, Beijing 100081, China.

E-mail address: [fanqunbo@bit.edu.cn](mailto:fanqunbo@bit.edu.cn) (Q. Fan).

22]. In addition, Tammas-Williams [23] used the laboratory X-ray microtomography to study the size, volume fraction, and spatial distribution of the pores in Ti–6Al–4 V components manufactured by selective electron beam melting. As the mass densities of constituent phases in dual-phase titanium alloys are very similar, it is difficult to distinguish the microstructure characteristics of the constituent phases from each other just by density thresholding. Fortunately, dual-energy micro-CT imaging has been recently proposed to distinguish the microstructure characteristics of the constituent phases, which is based on the difference in the X-ray absorption coefficient with different X-ray photon energies by materials [24]. Moreover, it has been widely applied in the biomedical field [25–27]. Hence, in the present study, dual-energy micro-computed tomography (Micro-CT) imaging was applied to obtain the 3D annealed microstructure images of TC6 dual-phase titanium alloy.

## 2. Material and methods

The chemical composition of as-received TC6 titanium alloy (Baoji Nonferrous Metal Works forged product, Baoji, China) is presented in Table 1. The main chemical compositions (wt%) are as follows:  $\alpha$ -phase stabilizing element 6Al and  $\beta$ -phase stabilizing elements 1.5Cr, 2.5Mo, and the bal. Ti.

In this study, specimens of TC6 titanium alloy for scanning electron microscope (SEM) and energy dispersive spectroscopy (EDS) were annealed at 800 °C for 2 h followed by air cooling. The surface perpendicular to the rolling direction was prepared with conventional metallographic grinding and polishing steps, and then etched with Kroll's reagent (2%HF, 10% HNO<sub>3</sub>, and 88%H<sub>2</sub>O) for a few seconds. The specimens designated for electron back scattered diffraction (EBSD) measurement must have a flat highly polished (mirror-finish) surface. In addition, the residual stress of the surface, owing to mechanical polishing, was removed via electro polishing at a voltage of 25 V, for ~30 s, in a solution of 6% per chloric acid (HCl<sub>4</sub>), 34% butan-1-ol (C<sub>4</sub>H<sub>9</sub>OH), and 60% methanol (HNO<sub>3</sub>) at 25 °C. The image processing and analysis software, CTAn V1.13 (Bruker microCT, Kontich, Belgium) was employed to perform 2D quantitative analysis of microstructure of TC6 titanium alloy. Furthermore, these experimental results serve as a reference to verify the accuracy of the following 3D microstructure model of TC6 titanium alloy obtained by laboratory X-ray microtomography.

The specimen of TC6 titanium alloy for X-ray tomogram was machined by wire electrical discharge machining. The shape and size are shown in Fig. 1, the top portion is the cylindrical scanning area with  $\varnothing 0.5 \times 1$  mm, and the bottom portion is a cylinder with  $\varnothing 4 \times 4$  mm performing as a supportive platform. It should be noted that the axial direction of the cylinder specimen is paralleled to the rolling direction in this study.

The dual-energy Micro-CT acquisition was performed by scanning the specimen twice with different X-ray filters and applied tube voltages. The specimen should not be moved between scans, whereas the image magnification and resolution should be the same [24]. The X-ray tomograms were performed using the Sky-Scan 1172 high-resolution desktop X-ray microtomography system (Bruker microCT, Kontich, Belgium). The main scanning measurement processes are shown in Fig. 2. Initially, the X-ray tube was

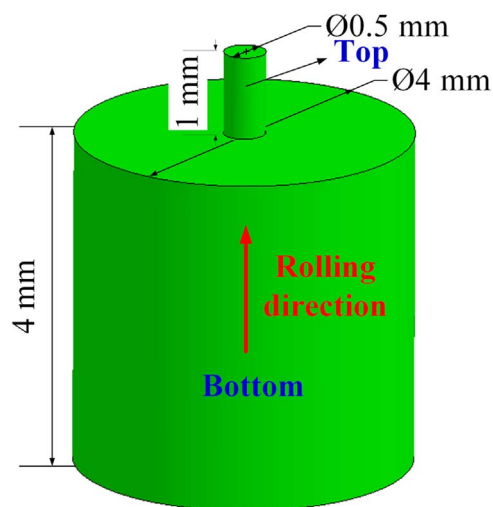


Fig. 1. Size and shape schematic of Micro-CT scanning specimen.

moved toward the specimen as close as possible to get a high resolution, and then a proper supply of voltage and current to the X-ray tube, as well as a filter, was set to obtain a high-contrast projection image. The specimen was placed on a rotary stage between the charge coupled device (CCD) detector and the X-ray tube, so that a projection image could be taken by the CCD detector at each angular position with step-by-step rotation of the specimen. Finally, a series of projection images with different angles were obtained.

The projection images was reconstructed by NRecon V1.6.10 (Bruker microCT, Kontich, Belgium) on the basis of the principle of Feldkamp back projection algorithm [11]. The reconstruction process produced a set of trans-axial greyscale 2D Micro-CT slices of the specimen. Then, the Micro-CT slices with different X-ray filters and applied tube voltages were imported into dual-energy Micro-CT imaging program Dehist (Bruker microCT, Kontich, Belgium) to enhance the absorption contrast between each constituent phase. Next, the processed Micro-CT slices with high-contrast and low-noise annealed microstructure of TC6 titanium alloy were imported into the Simpleware (Simpleware Ltd, Exeter, UK) to obtain the 3D microstructure of each constituent phase in TC6 titanium alloy. Eventually, the 3D microstructures of each constituent phase in TC6 titanium alloy was analyzed quantitatively by CTAn V1.13.

## 3. Results and discussion

The annealed microstructure of TC6 titanium alloy obtained by SEM is displayed in Fig. 3. It is observed that the annealed microstructure consists of  $\alpha$  phase (dark gray) with hexagonal close-packed (hcp) crystal structure and  $\beta$  phase (bright white) with body-centered cubic (bcc) crystal structure. The magnification of the frame-selected area in Fig. 3(a) is shown in Fig. 3(b). The  $\alpha$  phase is composed of equiaxed primary  $\alpha$  phase and secondary  $\alpha$  phase. Moreover, the secondary  $\alpha$  phase and  $\beta$  phase tangle together.

### 3.1. 2D quantitative analysis of microstructure and composition of TC6 titanium alloy

#### 3.1.1. Area fraction and grain size distribution of the primary $\alpha$ and $\beta$ phases of TC6 titanium alloy

It is feasible to separate the primary  $\alpha$  phase from the secondary  $\alpha$  and  $\beta$  phases based on the difference in shape and gray

Table 1

Chemical composition of as-received TC6 titanium alloy (wt%).

Al	Cr	Mo	Fe	Si	C	N	H	Ti
6	1.5	2.5	0.5	0.3	< 0.07	< 0.03	< 0.01	Bal.

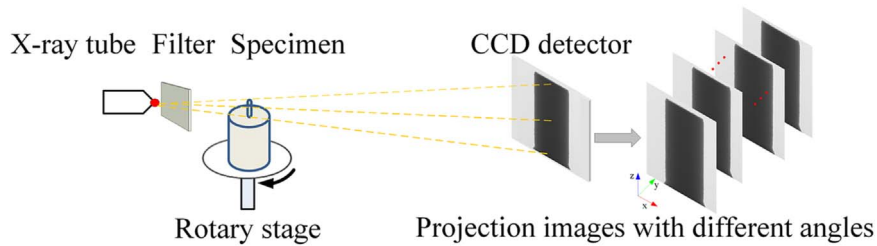


Fig. 2. The main process of scanning measurement.

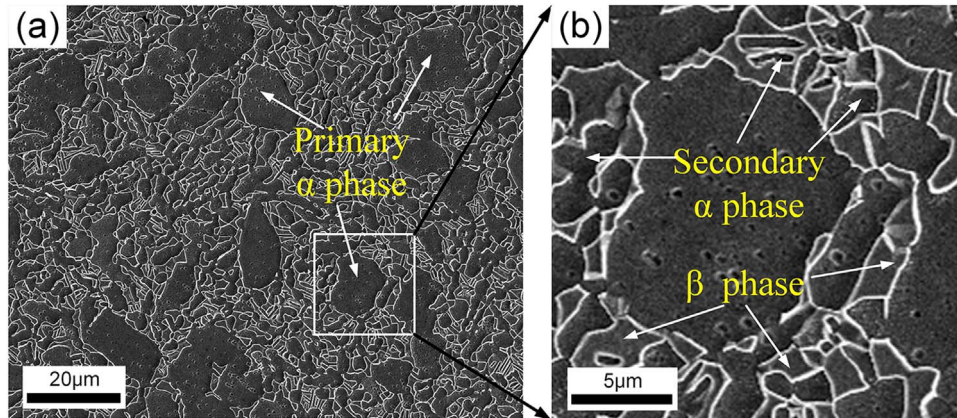


Fig. 3. SEM of annealed microstructure of TC6 titanium alloy.

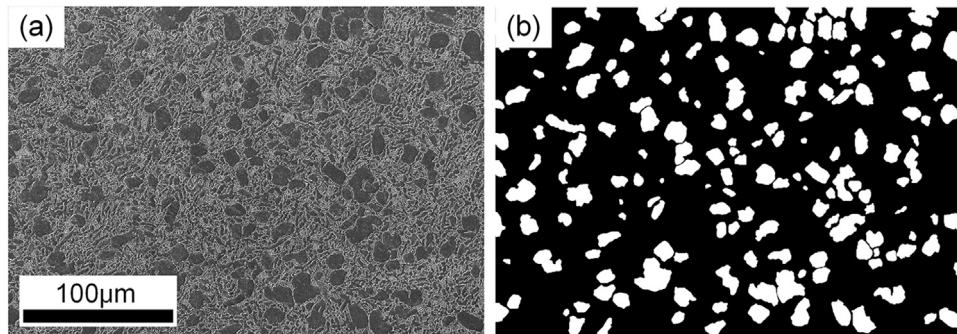


Fig. 4. Image binarization processing: (a) original SEM of TC6 titanium alloy; (b) image after binarization processing.

value. Fig. 4(a) shows the SEM of TC6 titanium alloy. The dark gray region indicates the  $\alpha$  phase mixing with the primary and secondary  $\alpha$  phases, and the bright white region indicates the  $\beta$  phase. The binary image of TC6 titanium alloy is obtained by the image processing software Photoshop, as shown in Fig. 4(b), and the corresponding operations are as follows. First, the SEM image was converted to 8-bit gray scale one. Second, smoothing filter (Gaussian Blur,  $R=4$ ) as well as shrinking and expand tools was applied on the 8-bit gray scale image to separate the primary  $\alpha$  phase from the secondary  $\alpha$  phase. Third, the magic wood tool (tolerance value of 5) was performed to select the primary  $\alpha$  phase. In the end, the gray value of selected area for primary  $\alpha$  phase was set to direct 255 (white), while the gray value of the rest area was set to 0 (black). In this way, the SEM image of TC6 titanium alloy was converted into the binary image. The white region indicates the primary  $\alpha$  phase with an area fraction of 23.7%, whereas the black region represents the secondary  $\alpha$  and  $\beta$  phases.

CTAn V1.13 was employed to obtain the primary  $\alpha$  phase grain size distribution histogram. As shown in Fig. 5, with the increase in the equivalent grain diameter of the primary  $\alpha$  phase grains, the corresponding frequency initially increases and then decreases. About 76% of the grains were 4–12  $\mu\text{m}$  in diameter, whereas the

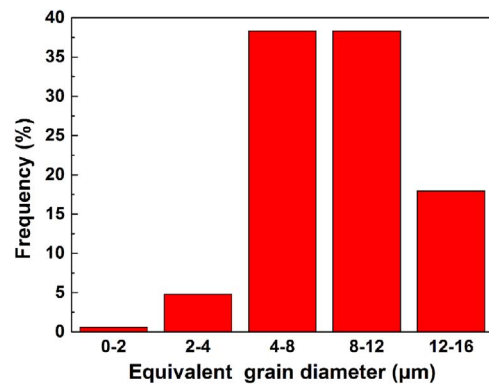
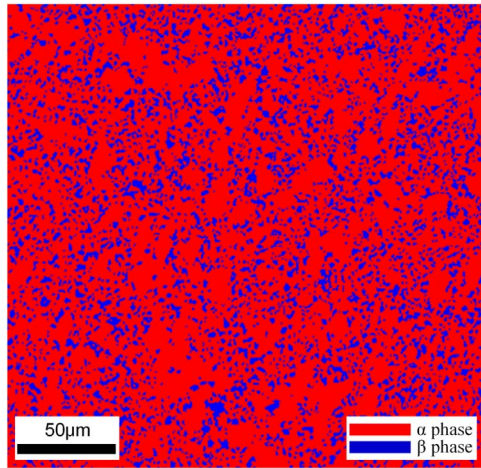


Fig. 5. Frequency distribution of the equivalent grain diameter of the primary  $\alpha$  phase grains.

corresponding frequency ranging from 0 to 4  $\mu\text{m}$  is the lowest, approximately 5%. Further analysis shows that the average equivalent grain diameter is 9.41  $\mu\text{m}$ .

The secondary  $\alpha$  phase and  $\beta$  phase of TC6 titanium alloy in SEM, as shown in Fig. 4(a), tangle together, making it hard to



**Fig. 6.** Phase distribution map of EBSD of TC6 titanium alloy: the red region indicates the  $\alpha$  phase composed of the primary and secondary  $\alpha$  phases, and the blue region indicates the  $\beta$  phase. (For interpretation of the references to color in this figure legend, the reader is referred to the web version of this article.)

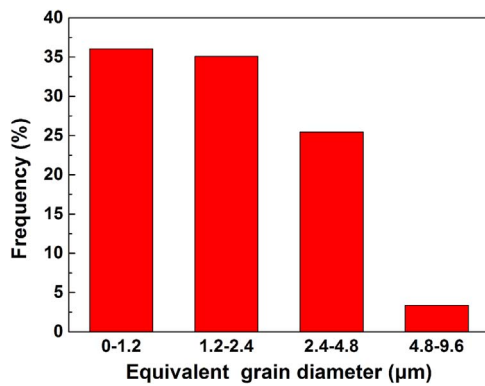


**Fig. 7.** Frequency distribution of the equivalent grain diameter of the  $\beta$  phase.

separate them by means of image processing. However, as EBSD technology typically yields the microstructure of alloys based on the difference of crystal structure types, it was applied to distinguish the  $\beta$  phase from the secondary  $\alpha$  phase in TC6 titanium alloy. Fig. 6 shows the phase distribution map of EBSD image of TC6 titanium alloy, the blue region indicates the  $\beta$  phase with an area fraction of 21.7% and the red region represents the mixture of the primary and secondary  $\alpha$  phases. On the basis of the area fractions of the primary  $\alpha$  phase and the  $\beta$  phase, the area fraction (54.6%) of the secondary  $\alpha$  phase is deduced.

The frequency distribution of the equivalent grain diameter of the  $\beta$  phase was obtained using CTAn V1.13. As shown in Fig. 7,

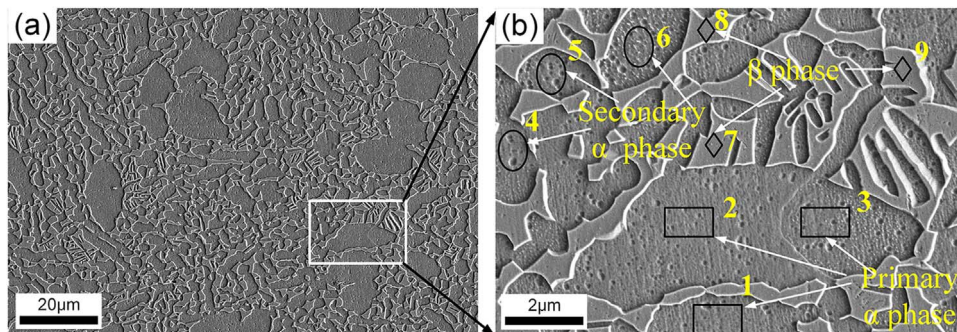


**Fig. 8.** EDS analysis sections of TC6 titanium alloy by SEM: the region in rectangular frames represents the primary  $\alpha$  phase, the region in rhombus frames represents the secondary  $\alpha$  phase, and the region in ellipse frames represents the  $\beta$  phase.

**Table 2**

Element weight percentage and density of each constituent phase in TC6 titanium alloy.

Constituent phase	Al (wt%)	Cr (wt%)	Mo (wt%)	Ti (wt%)	Density (g/cm <sup>3</sup> )
Primary $\alpha$ phase	7.12	0.81	0.82	91.25	4.47
Secondary $\alpha$ phase	6.44	1.35	1.94	90.27	4.56
$\beta$ phase	3.62	2.7	5.71	87.97	4.86

**Table 3**

Dual-energy Micro-CT Scanning parameters of TC6 titanium alloy.

Voltage (kV)	Current ( $\mu\text{A}$ )	Filter	Rotation step ( $^{\circ}$ )	Resolution ( $\mu\text{m}$ )
59	167	0.5 mmAl	0.6	0.6
100	100	0.5 mmAl+0.5 mmCu	0.6	0.6

with an increase of the equivalent grain diameter of the  $\beta$  phase, the corresponding frequency shows a descending trend gradually. The frequency of the equivalent grain diameter ranging from 0 to 2.4  $\mu\text{m}$  peaks at 71.1%, whereas the corresponding frequency ranging from 4.8 to 9.6  $\mu\text{m}$  is the lowest, approximately 3.4%. Further analysis shows that the average equivalent grain diameter of the  $\beta$  phase is 2.34  $\mu\text{m}$ .

### 3.1.2. Quantitative analysis for chemical composition of each constituent phase of TC6 titanium alloy

The density difference among the constituent phases of TC6 titanium alloy needs to be verified as the computer 3D visualization of Micro-CT is based on the density contrast of materials. The sections of EDS analysis by SEM are shown in Fig. 8. Numbers 1–3, 4–6, and 7–9 represent the sections of EDS analysis in the primary  $\alpha$  phase, secondary  $\alpha$  phase, and  $\beta$  phase, respectively.

The average weight percentages of the main elements in the corresponding constituent phase were obtained by the ones in the relevant positions of EDS analysis. Then, they were imported into Eq. (1) to obtain the mass density of each constituent phase:

$$\rho_{\text{phase}} = \sum w_i \times \rho_i \quad (1)$$

$\rho_{\text{phase}}$  is the density of the constituent phase,  $w_i$  is the weight percentage of the element  $i$ , and  $\rho_i$  is the density of the element  $i$ . In this study, the densities of the elements of aluminum, chromium, molybdenum, and titanium are 2.694, 7.18, 10.20, 4.53 g/cm<sup>3</sup>, respectively.

The weight percentages of the main elements and the densities of the corresponding constituent phases are presented in Table 2. In the primary  $\alpha$  phase, the weight percentage of low-density element aluminum is higher (up to 7.12%), whereas that of the

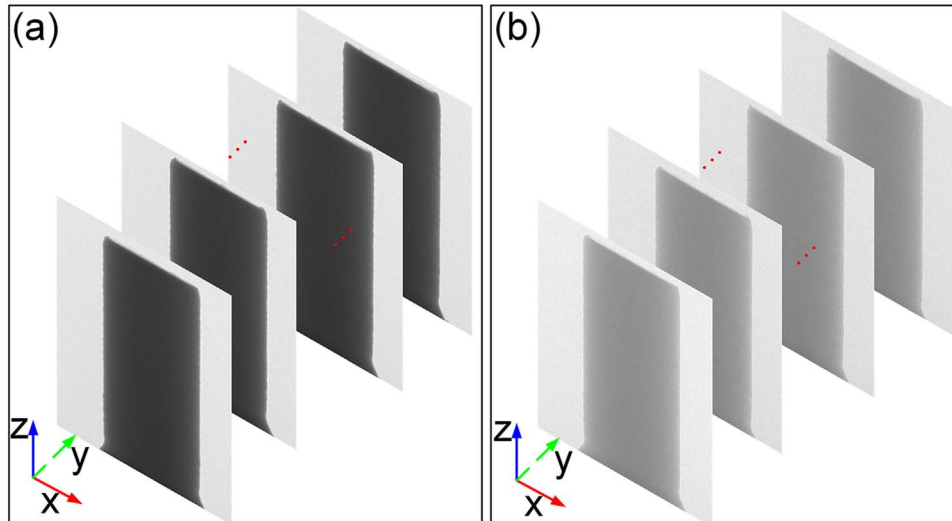


Fig. 9. Projection images with different X-ray tube voltages: (a) 59 kV; (b) 100 kV.

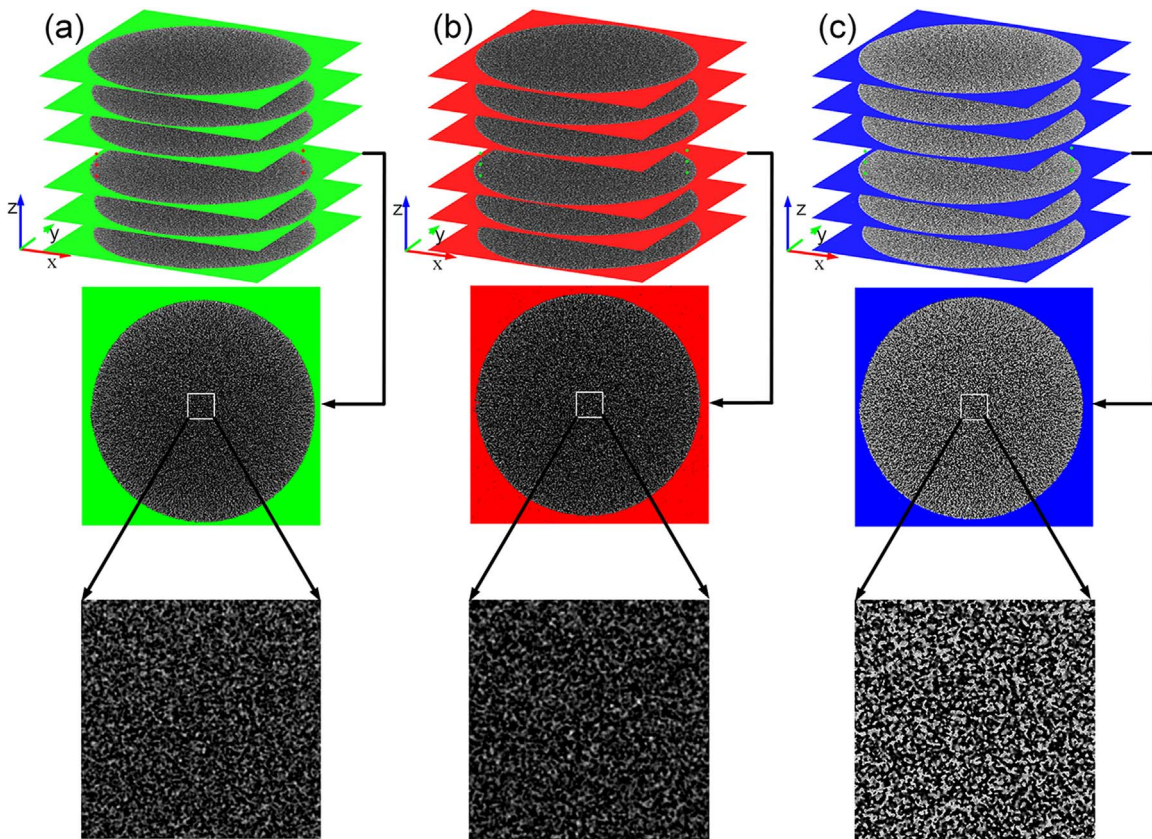


Fig. 10. Micro-CT slices with pre- and post-dual-energy imaging: (a) unprocessed images (59 kV); (b) unprocessed images (100 kV); (c) processed images.

high-density elements such as chromium and molybdenum are lower (just 0.81% and 0.82%, respectively); hence, its density is the lowest. In the  $\beta$  phase, however, the weight percentages of high-density elements, such as chromium and molybdenum, increase to 2.7% and 5.71%, respectively; hence, its density is the highest among all the constituent phases. The density of the secondary  $\alpha$  phase is 2.01% more than the primary  $\alpha$  phase, but is 6.6% less than the  $\beta$  phase. From the above results, it is concluded that the primary and secondary  $\alpha$  phases have the more similar absorption coefficients. Therefore, it is hard to obtain the 3D microstructures of constituent phases in TC6 titanium alloy by traditional single scan Micro-CT. In order to overcome the difficulty, dual-energy

Micro-CT imaging was employed in this study to enhance the absorption contrast among the constituent phases of TC6 titanium alloy.

### 3.2. 3D microstructural reconstruction and quantitative characterization of TC6 titanium alloy based on dual-energy Micro-CT technique

Any given material will have different absorption coefficients when imaged by Micro-CT technique at low and high X-ray energies, resulting in a predictable change in the absorption when imaged by two known X-ray energies [24]. Dual-energy Micro-CT

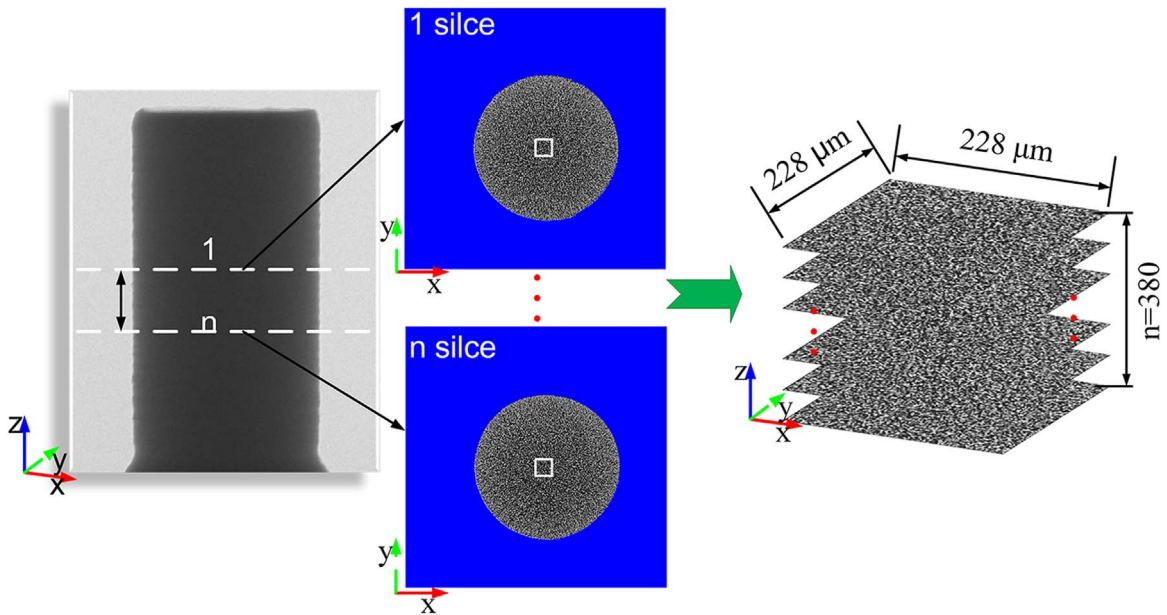


Fig. 11. Schematic of selecting the interesting volume in Micro-CT slices.

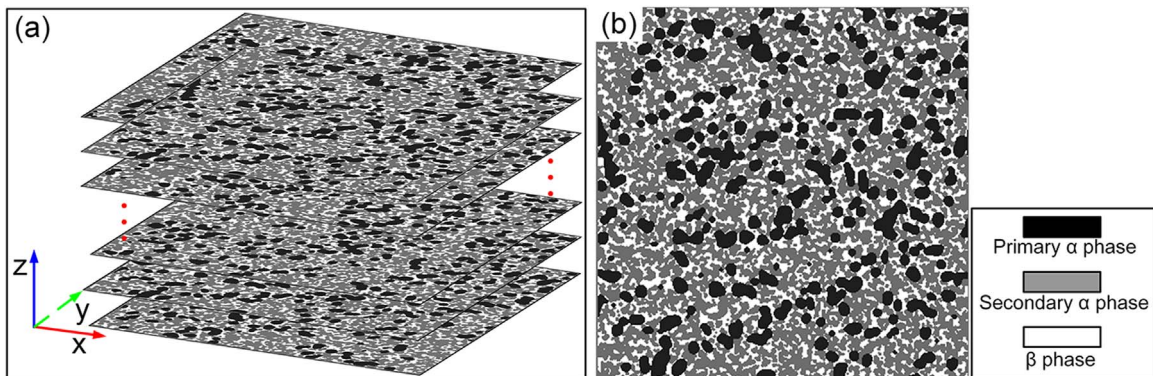


Fig. 12. (a) VOI Micro-CT slices after image processing; (b) the corresponding representative Micro-CT slice.

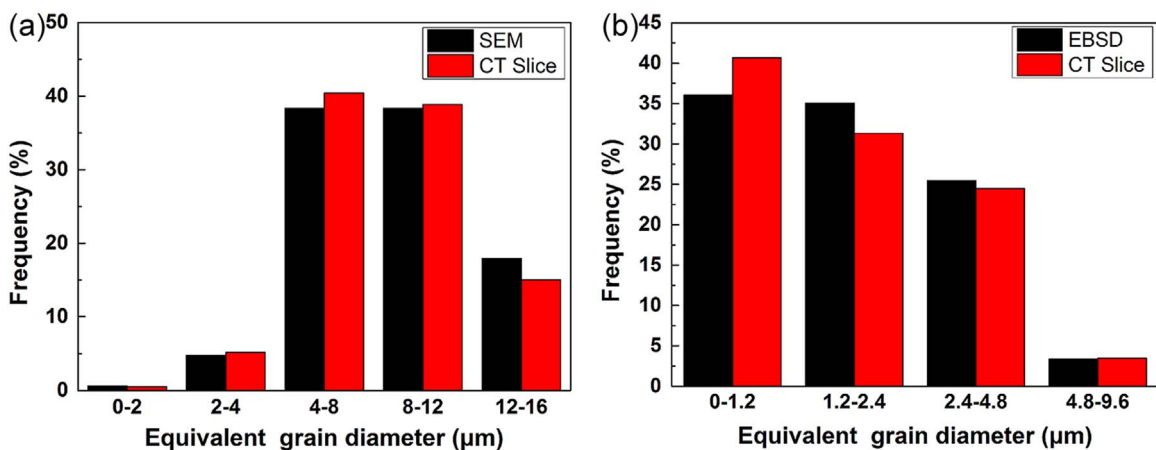


Fig. 13. Frequency distribution of the equivalent grain diameter of the constituent phases in TC6 titanium alloy between traditional microscopy and representative Micro-CT slice for: (a) primary  $\alpha$  phase; (b)  $\beta$  phase.

imaging program Dehist is based on the above principle to distinguish the constituent phases of TC6 titanium alloy with similar absorption coefficients on the same X-ray energy but different chemical compositions from one another by analyzing their energy dependent changes in absorption.

### 3.2.1. Dual-energy X-ray tomography

In Table 3, two sets of scanning parameters with the same rotation step of  $0.6^\circ$  and resolution of  $0.6 \mu\text{m}$  are shown with the following conditions: the X-ray tube voltages are 59 kV and 100 kV and the applied X-ray filters are 0.5 mm Al and 0.5 mm Al+0.5 mm Cu for set 1 and set 2, respectively. The projection images of the

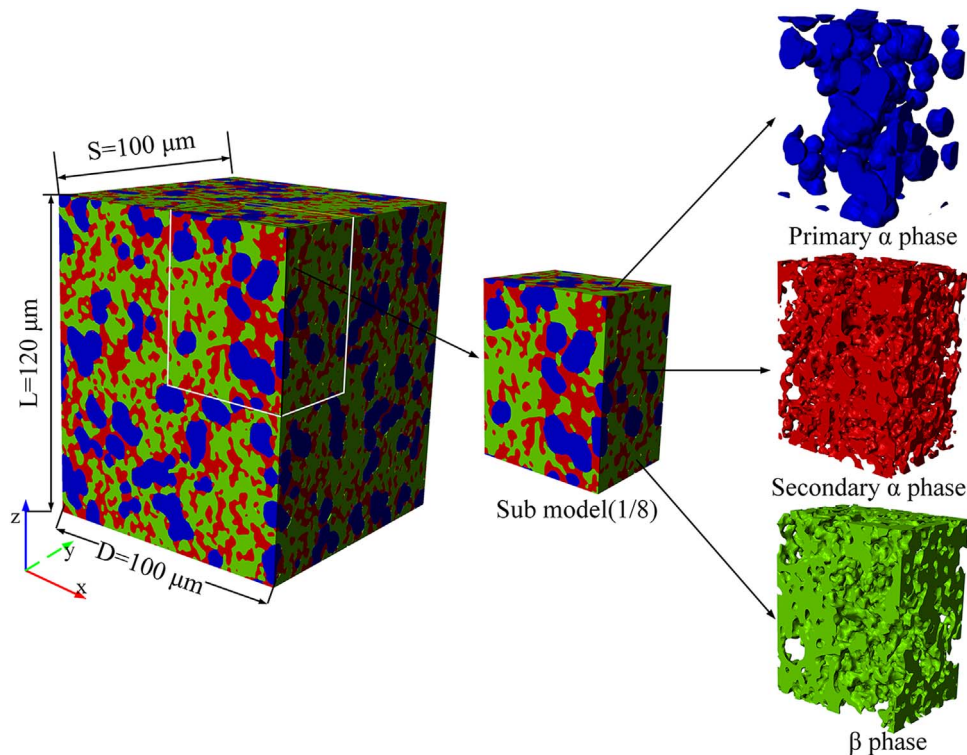
**Table 4**

The area fractions and the average equivalent grain diameters and their corresponding errors for the primary  $\alpha$  and  $\beta$  phases between traditional microscopy and representative Micro-CT slice.

Phase	Area fraction (%)		Absolute deviation (%)	Average equivalent grain diameter ( $\mu\text{m}$ )		Absolute deviation ( $\mu\text{m}$ )
	CT slice	Micrograph		CT slice	Micrograph	
Primary $\alpha$ phase	24.8	23.7	1.1	9.21	9.41	0.2
$\beta$ phase	22.6	21.7	0.9	2.27	2.34	0.07

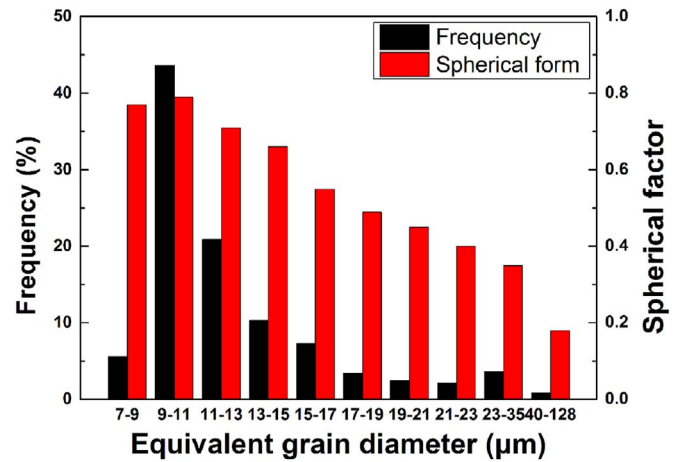
specimen with high and low voltages are shown in Fig. 9.

Fig. 10 shows the Micro-CT slices of the specimen with pre- and post-dual-energy imaging. The projection images with different voltages, shown in Fig. 10, were imported into NRecon to obtain the corresponding Micro-CT slices. The low energy Micro-CT slices have more noise, but show the constituent phases with better contrast (seeing Fig. 10(a)), whereas the high energy ones show clearer borders, but lower contrast (seeing Fig. 10(b)). In addition to independent evaluation of the separate energy-level slices, it is possible to mathematically mix the two energy-level slices to yield a single “blended” slices [28–30] that therefore balance the advantages and disadvantages of both low and high energy slices according to the attenuation difference between the constituent phases in TC6 titanium alloy. The process enhancing the absorption contrast between each constituent phase in TC6 titanium alloy by dual-energy Micro-CT imaging program Dehist [31] is as follows: once the two datasets of Micro-CT slices at different filter and voltage settings were loaded both at the same cross-section level, segmentation lines should be applied to the dual-energy gray histogram plot. Placing the T-bar (segmentation lines are in a “T” shape) between appropriate regions (thresholds: 71–33, slope:  $311.184^\circ$ ) in the dual energy plot would achieve the dual energy

**Fig. 14.** 3D microstructure model of each constituent phase in TC6 titanium alloy.**Table 5**

The quantitative analysis results of the 3D microstructure model of TC6 titanium alloy.

Phase	Volume ( $\mu\text{m}^3$ )	Surface area ( $\mu\text{m}^2$ )	Volume fraction (%)	Surface-volume ratio ( $\mu\text{m}^{-1}$ )
Primary $\alpha$ phase	$6.61 \times 10^5$	$3.11 \times 10^6$	28.32	0.66
Secondary $\alpha$ phase	$1.12 \times 10^6$	$1.09 \times 10^6$	47.78	0.98
$\beta$ phase	$5.58 \times 10^5$	$1.18 \times 10^6$	23.90	2.12

**Fig. 15.** Frequency and spherical factor of the equivalent grain diameter of primary  $\alpha$  phase.

segmentation. Thereof, a third weighted-average Micro-CT slices (seeing Fig. 10(c)) was reconstructed from both single-energy datasets of slices (seeing Fig. 10(a and b)). Then, the slices with different voltages were imported into dual-energy Micro-CT imaging

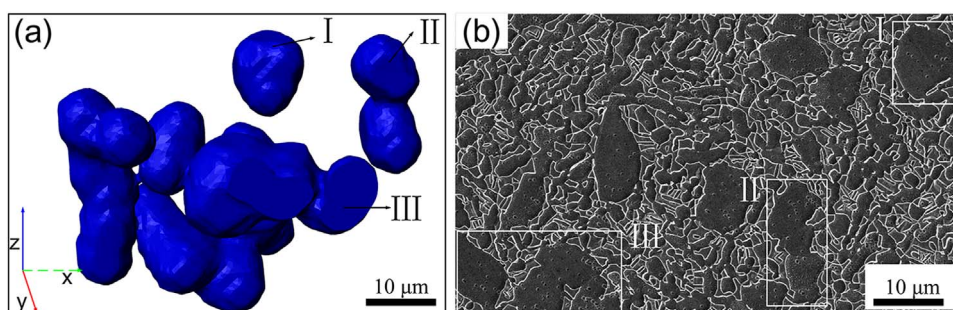


**Fig. 16.** Morphology of primary  $\alpha$  phase in the 3D microstructure model and SEM: (a) primary  $\alpha$  phase in 3D space; (b) SEM of TC6 titanium alloy.

program Dehist to enhance the absorption contrast between each constituent phase (seeing Fig. 10(c)). A Micro-CT slice was taken from the middle of trans-axial of the specimen to give a better indication of the differences between pre- and post-dual-energy imaging. It is obvious that the post-dual-energy imaging Micro-CT slice exhibits higher contrast and signal-to-noise ratio compared with the pre-dual-energy imaging ones.

### 3.2.2. Reliability verification of Micro-CT slices

Considering the efficiency of the following data processing, the volume-of-interest (VOI) of the Micro-CT slices (seeing Fig. 10(c)) was selected initially. As is shown in Fig. 11, a total of 380 slices were selected in the z-axis direction (through trans-axial direction), whereas a region of  $228 \mu\text{m} \times 228 \mu\text{m}$  was selected in the xy plane (frame-selected area).

Then, these VOI Micro-CT slices were imported into CTAn to perform image processing, such as filtering, smoothing and noise reducing. Fig. 12(a) is the VOI Micro-CT slices after image processing. Fig. 12(b) is the representative Micro-CT slice taken from the center of the VOI Micro-CT slices: the white, gray, and black regions indicate the  $\beta$  phase, the secondary  $\alpha$  phase, and the primary  $\alpha$  phase, respectively.

Then, the 2D quantitative analysis for area fraction and size distribution of each constituent phase was performed and compared with the micrographic results in Section 2. 1. As shown in Fig. 13, the results reveal good agreement. For the primary  $\alpha$  phase, the frequency difference of the equivalent grain diameter between the representative CT slice and SEM ranges from 0.3% to 3%; for the  $\beta$  phase, the frequency difference is limited to less than 4%.

Table 4 displays the area fractions and average equivalent grain diameters of constituent phases of the micrograph and representative Micro-CT slice and their corresponding absolute deviations. The absolute deviations of area fraction are 1.1% and 0.9% for the primary  $\alpha$  phase and  $\beta$  phase, respectively. Correspondingly, the absolute deviations of average equivalent grain diameter are  $0.2 \mu\text{m}$  and  $0.07 \mu\text{m}$ , respectively. Therefore, the reliability of Micro-CT slices could be confirmed.

### 3.2.3. Quantitative characterization of the 3D microstructure model

The Micro-CT slices processed by dual-energy imaging were imported into the Simpleware to reconstruct the 3D microstructure of each constituent phase in TC6 titanium alloy. As shown in Fig. 14, the size of the 3D microstructure model is  $120 \times 100 \times 100 \mu\text{m}$ . To analyze the 3D microstructure characteristics of TC6 titanium alloy at a finer scale, one eighth of the model was selected and the 3D models of primary and secondary  $\alpha$  phases as well as  $\beta$  phase were displayed independently. The primary  $\alpha$  phase is composed of discrete equiaxed grains and interconnected grains; the secondary  $\alpha$  phase and  $\beta$  phases form a completely interconnected network in 3D space. The reason for the 3D microstructure of the secondary  $\alpha$  phase appearing as an interconnected network instead of a lamellar structure is related

to the heat treatment process of TC6 titanium alloy. In this study, the specimen was achieved by annealing at  $800 \text{ }^\circ\text{C}$  for 2 h followed by air cooling. During the holding stage, the secondary alpha phase dissolves, and nucleates back at grain boundaries or inside the  $\beta$  grains [32,33] during air-cooling down to the room temperature from  $\beta + \alpha$  region, and interconnects with the retained  $\beta$  phase forming a completely interconnected network.

Table 5 gives the quantitative analysis results of the 3D microstructure model such as the volume, surface area, volume fraction, and surface-volume ratio (SVR) of each constituent phase in TC6 titanium alloy. For the volume fraction, the secondary  $\alpha$  phase is the highest, 47.78%. The primary  $\alpha$  phase takes the second place, 28.32%, and the  $\beta$  phase is the lowest, 23.90%. Moreover, for the SVR, the  $\beta$  phase is the highest,  $2.12 \mu\text{m}^{-1}$ , whereas the primary  $\alpha$  is the lowest,  $0.66 \mu\text{m}^{-1}$ . It is obvious that the above information can hardly be obtained in traditional 2D microscopy technology.

For further analyzing the morphology and connectivity of the primary  $\alpha$  phase in 3D space, the histograms of frequencies as well as spherical factors with different equivalent sphere diameter ranges are shown in Fig. 15. With the increase in the equivalent sphere diameter, the corresponding frequency quickly reaches the peak at 43.2% in range of 9–11  $\mu\text{m}$ , and then decreases gradually. Similarly, the spherical factor also increases initially, and then decreases. The average spherical factors are 0.75 and 0.78, respectively, in the equivalent sphere diameter range of 7–9  $\mu\text{m}$  and 9–11  $\mu\text{m}$ , which means that the microstructure of primary  $\alpha$  phase exists in the form of discrete equiaxed grains in range of 7–11  $\mu\text{m}$ . As the equivalent sphere diameter increases, the spherical factor decreases gradually from 0.78 to 0.18, revealing that the microstructure of primary  $\alpha$  phase at larger grain sizes exists in the form of interconnected grains.

Fig. 16 shows a direct comparison of the morphology of the primary  $\alpha$  phase between the 3D microstructure model and SEM. In Fig. 16(a), the primary  $\alpha$  grains exist with three forms: individual equiaxed grain (I), two grains with overlapping edges (II), and multiple grains with overlapping edges (III). The corresponding phenomenon is also illustrated in Fig. 16(b) (see the white rectangles: I, II, and III).

## 4. Conclusions

In the present study, Micro-CT slices with high-contrast and low-noise annealed microstructure of TC6 titanium alloy were achieved by laboratory X-ray microtomography by employing dual-energy Micro-CT imaging. It overcame the difficulty of low absorption contrast on account of the similarity in density between the primary  $\alpha$  and  $\beta$  phases in TC6 titanium alloy. Furthermore, the validity of Micro-CT slices of TC6 titanium alloy was proved by comparing the results between a representative Micro-CT slice and a traditional microscopy image. Then, the 3D

microstructures of each constituent phase in TC6 titanium alloy were reconstructed and a quantitative analysis was done. The results show that the primary  $\alpha$  phase was composed of individual equiaxed grains and interconnected grains, and the fraction of the individual equiaxed grains was up to 50%; the secondary  $\alpha$  phase formed a completely interconnected network in 3D space instead of a lamellar structure with the highest volume fraction of 47.78%, as it nucleates and grows from the  $\beta$  phase matrix in large quantities during the process of annealing; the morphology distribution of  $\beta$  phase was similar to the secondary  $\alpha$  phase, forming a completely interconnected network in 3D space, and its volume fraction is the lowest, 23.90%.

## Acknowledgments

We gratefully acknowledge the funding support from project 51571031 of the Chinese National Natural Science Foundation. The assistance of Application Engineer. Michael Sun of Micro Technology Hong Kong Ltd. with dual-energy Micro-CT imaging aspects is greatly appreciated.

## References

- [1] Z. Tarzimgohadam, S. Sandlöbes, K.G. Pradeep, D. Raabe, Microstructure design and mechanical properties in a near- $\alpha$  Ti-4Mo alloy, *Acta Mater.* 97 (2015) 291–304.
- [2] R. Filip, K. Kubiak, W. Ziąja, J. Sieniawski, The effect of microstructure on the mechanical properties of two-phase titanium alloys, *J. Mater. Process. Technol.* 133 (2003) 84–89.
- [3] J. Sieniawski, R. Filip, W. Ziąja, The effect of microstructure on the mechanical properties of two-phase titanium alloys, *Mater. Des.* 18 (1997) 361–363.
- [4] J. Chrapoński, W. Szkliniarz, Quantitative metallography of two-phase titanium alloys, *Mater. Charact.* 46 (2001) 149–154.
- [5] M.V. Kral, M.A. Mangan, G. Spanos, R.O. Rosenberg, Three-dimensional analysis of microstructures, *Mater. Charact.* 45 (2000) 17–23.
- [6] M.R. Baldissera, P.R. Rios, L.R.O. Hein, H.R.Z. Sandim, Three-dimensional characterization of pores in Ti-6Al-4V alloy, *Mater. Res.* 14 (2011) 102–106.
- [7] J.E. Spowart, Automated serial sectioning for 3-D analysis of microstructures, *Scr. Mater.* 55 (2006) 5–10.
- [8] H. Singh, A.M. Gokhale, Y. Mao, A. Tewari, A.K. Sachdev, Reconstruction and quantitative characterization of multiphase, multiscale three-dimensional microstructure of a cast Al-Si base alloy, *Metall. Mater. Trans. B* 40 (2009) 859–870.
- [9] N. Vanderesse, E. Maire, M. Darrieulat, F. Montheillet, M. Moreaud, D. Jeulin, Three-dimensional microtomographic study of Widmanstätten microstructures in an alpha/beta titanium alloy, *Scr. Mater.* 58 (2008) 512–515.
- [10] J. Kastner, B. Harrer, H.P. Degischer, High resolution cone beam x-ray computed tomography of 3D-microstructures of cast Al-alloys, *Mater. Charact.* 62 (2011) 99–107.
- [11] J. Kastner, B. Harrer, G. Requena, O. Brunke, A comparative study of high resolution cone beam x-ray tomography and synchrotron tomography applied to Fe- and Al-alloys, *NDT E Int.* 43 (2010) 599–605.
- [12] E. Maire, P.J. Withers, E. Maire, Quantitative x-ray tomography, *Int. Mater. Rev.* 59 (2014) 1–43.
- [13] E. Maire, J.C. Grenier, D. Daniel, A. Baldacci, H. Klöcker, A. Bigot, Quantitative 3D characterization of intermetallic phases in an Al-Mg industrial alloy by x-ray microtomography, *Scr. Mater.* 55 (2006) 123–126.
- [14] S.S. Singh, C. Schwartzstein, J.J. Williams, X. Xiao, F. De Carlo, N. Chawla, 3D microstructural characterization and mechanical properties of constituent particles in Al 7075 alloys using x-ray synchrotron tomography and nanoindentation, *J. Alloy. Compd.* 602 (2014) 163–174.
- [15] F. Baino, C. Vitale-Brovarone, Mechanical properties and reliability of glass-ceramic foam scaffolds for bone repair, *Mater. Lett.* 118 (2014) 27–30.
- [16] P. Marcián, Z. Majer, Z. Florian, I. Dlouhý, Stress strain analysis of high porous ceramics, *Adv. Mater. Res.* 482 (2012) 1330–1333.
- [17] C. Madonna, B.S. Almqvist, E.H. Saenger, Digital rock physics: numerical prediction of pressure-dependent ultrasonic velocities using Micro-CT imaging, *Geophys. J. Int.* 189 (2012) 1475–1482.
- [18] G. Zacher, M. Halisch, P. Westenberger, T. Paul, T. Tan, Quantitative investigation of microstructures within porous rocks by using very high resolution x-ray micro-CT imaging, in: *Proceedings of the EAGE/FESM Joint Regional Conference Petrophysics Meets Geoscience*, 2014.
- [19] L.-M. Ren, T. Arahira, M. Todo, H. Yoshikawa, A. Myoui, Biomechanical evaluation of porous bioactive ceramics after implantation: micro CT-based three-dimensional finite element analysis, *J. Mater. Sci.: Mater. Med.* 23 (2012) 463–472.
- [20] Y. Feng, Z. Feng, S. Li, W. Zhang, X. Luan, Y. Liu, L. Cheng, L. Zhang, Micro-CT characterization on porosity structure of 3D Cf/SiCm composite, *Compos. Part A: Appl. Sci. Manuf.* 42 (2011) 1645–1650.
- [21] L.P. Djukic, G.M. Pearce, I. Herszberg, M.K. Bannister, D.H. Mollenhauer, Contrast enhancement of microCT scans to aid 3D modelling of carbon fibre fabric composites, *Appl. Compos. Mater.* 20 (2013) 1215–1230.
- [22] G. Li, X. Zhang, Q. Fan, L. Wang, H. Zhang, F. Wang, Y. Wang, Simulation of damage and failure processes of interpenetrating SiC/Al composites subjected to dynamic compressive loading, *Acta Mater.* 78 (2014) 190–202.
- [23] S. Tammas-Williams, H. Zhao, F. Léonard, F. Derguti, I. Todd, P.B. Prangnell, XCT analysis of the influence of melt strategies on defect population in Ti-6Al-4V components manufactured by selective electron beam melting, *Mater. Charact.* 102 (2015) 47–61.
- [24] L.A. Fitri, V. Asyana, T. Ridwan, F. Anwar, H. Soekersi, F.D.E. Latief, F. Haryanto, Dual energy micro CT SkyScan 1173 for the characterization of urinary stone, in: *Proceedings of the 13th South-East Asian Congress of Medical Physics*, 2016.
- [25] F. Kelcz, P.M. Joseph, S.K. Hilal, Noise considerations in dual energy CT scanning, *Med. Phys.* 6 (1979) 418–425.
- [26] M. Depypere, J. Nuyts, N. van Gestel, G. Carmeliet, F. Maes, P. Suetens, An iterative dual energy CT reconstruction method for a K-edge contrast material, *Med. Imaging* (2011).
- [27] L. G-M, W. S-Y, B.M. Yeh, Z. L-J, Dual-energy computed tomography in pulmonary embolism, *Br. J. Radiol.* 83 (2010) 707–718.
- [28] J. Paul, R.W. Bauer, W. Maentele, T.J. Vogl, Image fusion in dual energy computed tomography for detection of various anatomic structures—effect on contrast enhancement, contrast-to-noise ratio, signal-to-noise ratio and image quality, *Eur. J. Radiol.* 80 (2011) 612–619.
- [29] D.R. Holmes 3rd, J.G. Fletcher, A. Apel, J.E. Huprich, H. Siddiki, D.M. Hough, B. Schmidt, T.G. Flohr, R. Robb, C. McCollough, M. Wittmer, C. Eusemann, Evaluation of non-linear blending in dual-energy computed tomography, *Eur. J. Radiol.* 68 (2008) 409–413.
- [30] C. Eusemann, D.R. Holmes, T.G. Flohr, R. Robb, C. McCollough, Dual energy CT: how to best blend both energies in one fused image? *Prog. Biomed. Opt. Imaging* 6918 (2008) 691803–691810.
- [31] Enhanced contrast by dual-energy MicroCT imaging. (<http://bruker-microct.com/products/downloads.htm/>), 2013.
- [32] C. Cayron, Importance of the  $\alpha \rightarrow \beta$  transformation in the variant selection mechanisms of thermomechanically processed titanium alloys, *Scr. Mater.* 59 (2008) 570–573.
- [33] E. Aeby-Gautier, F. Bruneseaux, J. Da Costa Teixeira, B. Appolaire, G. Geandier, S. Denis, Microstructural formation in Ti alloys: in-situ characterization of phase transformation kinetics, *J. Miner. Met. Mater. Soc.* 59 (2007) 54–58.